

Nanocellulose films with combined cellulose nanofibers and nanocrystals: tailored thermal, optical and mechanical properties

Xiuxuan Sun · Qinglin Wu · Xiuqiang Zhang · Suxia Ren · Tingzhou Lei · Wencai Li · Guangyin Xu · Quanguo Zhang

Received: 21 August 2017 / Accepted: 15 December 2017 / Published online: 19 December 2017
© Springer Science+Business Media B.V., part of Springer Nature 2017

Abstract Cellulose nanofibers (CNFs) and nanocrystals (CNCs) were prepared, and used to prepare thin CNF/CNC films. Rheological behavior of CNF/CNC suspensions and the other relevant properties of the films were characterized in comparison with a commercial porous polymer battery separator (PBS) film of similar thickness. The use of mixed CNFs and CNCs in the film-forming suspension led to significant variation of film morphology, and structural properties. With the addition of CNCs in hybrid nanocellulose material, the CNF/CNC suspension viscosity and zeta potential, film tensile strength, crystallinity index, and optical transparency were increased. With the increased CNF loading in the suspension, film porosity, thermal stability, and

thermal expansion were enhanced. The CNF/CNC films exhibited better thermal stability, thermal expansion behavior, and optical properties than those of the commercial PBS film. The coefficient thermal expansion of the CNF/CNC and PBS films were 11.86–17.65 and 178.90 ppm/k, respectively. The CNF/CNC films had more uniform strength along all directions, whereas PBS film demonstrated anisotropic property. This work paves a new strategy to tailor the properties of nanocellulose based films.

Keywords Nanocellulose · Rheology · Film forming · Strength · Stability · Thermal expansion

Electronic supplementary material The online version of this article (<https://doi.org/10.1007/s10570-017-1627-9>) contains supplementary material, which is available to authorized users.

X. Sun · Q. Wu (✉)
School of Renewable Natural Resources, Louisiana State University AgCenter, Baton Rouge, LA 70803, USA
e-mail: qwu@agcenter.lsu.edu

X. Zhang · S. Ren · T. Lei
Key Biomass Energy Laboratory of Henan Province, Zhengzhou 450008, Henan, People's Republic of China

W. Li · G. Xu · Q. Zhang
Collaborative Innovation Center of Biomass Energy, Henan Agricultural University, Zhengzhou 450002, People's Republic of China

Introduction

Cellulose is considered as the most abundant renewable polymeric material in the world. Pure cellulose can be extracted from various biomass sources including wood, straw, sugar beet, and bacterial cellulose (Moon et al. 2011). Due to its high availability, biodegradability, low cost, high specific mechanical strength and easiness for modification, cellulose has been widely used in different forms for various applications (Habibi et al. 2010; Moon et al. 2011; Sun et al. 2016). In recent years, nanocellulose, including cellulose nanofibers (CNFs) and cellulose nanocrystals (CNCs) extracted from cellulose, has emerged as a versatile “green” nanomaterial

(Garusinghe et al. 2017; Linvill et al. 2017; Xu et al. 2017). Among many applications, CNFs and CNCs have been used to prepare thin films for use in food packaging, wound dressing, and energy devices (Herrera et al. 2016, 2017; Hollertz et al. 2017; Kumar and Christopher 2017). For example, nanocellulose films with different cellulose types was prepared and used to replace plastic film in low-moisture greasy food packaging (Shi et al. 2016). Amorphous cellulose film was prepared to replace cellophane in packaging, which exhibited seven times higher hydrolysis rate than that of cellophane (Zhang et al. 2015a). In the biomedical field, the biocompatibility of cellulose was most widely utilized. Nanocellulose film exhibited similar performance in the cell adhesion when compared with the conventional tissue engineering material (i.e., thermanox—TMX) (Hua et al. 2014). In addition, cellulose microfiber composite films were fabricated for use in a flexible hybrid piezoelectric generator (Alam and Mandal 2016). CNF paper-derived film was produced through vacuum filtration method and used to replace conventional porous polymer battery separator (PBS) films (Chun et al. 2012). Similarly, foldable organic-light-emitting diodes were fabricated with regenerated nanocellulose film, which showed an excellent thermal stability and a higher processing temperature (Zhu et al. 2013). Due to the flexibility, high transmittance, and low thermal expansion of CNC films, CNC films were considered as an alternative substrate to replace conventional conducting glass substrates in polymer solar cells fields (Costa et al. 2016).

Different applications require target-specific properties of nanocellulose film. For example, the criteria for the film in organic solar cell substrate are high optical transparency and high haze. Nanocellulose film with a 96% transparence and 60% haze were fabricated, which helped increase the power conversion efficiency of solar cells to about 10% (Fang et al. 2014). However, low optical haze is needed when nanocellulose films are applied into light emitting diode (LED) or touch screens (Zhu et al. 2013). The packaging industry requires films with low water vapor permeability (WVP), whereas high permeability is better for wound dressing application (Lin et al. 2013). In order to improve the barrier properties, different approaches have been investigated. For example, binary and ternary nanocomposites were prepared by mixing silver nanoparticles or poly(3-

hydroxybutyrate-co-3-hydroxyvalerate) (PHBV) with CNC suspension for potential application in food packaging (Zhang et al. 2017). ZnO nanocrystals were also used as an additive to fabricate CNC-ZnO nanohybrids, which increased the water uptake values by 126% for a wound dressing material (Abdalkarim et al. 2017). Due to the different shape and aspect ratio of CNFs and CNCs, the films prepared with different CNF/CNC mixing ratios can exhibit different morphological, thermal, optical and mechanical properties. In one related work (Xu et al. 2016), the haze and total transmittance properties of hybrid cellulose nanopaper were varied by changing CNF/CNC ratio (increased transparency and decreased haze with the addition of CNCs). Even though much work on the utilization of cellulose films in energy storage materials has been done (mainly focusing on the electrical/chemical properties), no detailed analysis on film forming mechanism and structural properties with various CNC and CNF materials has been reported. Additional work is thus highly needed to understand the CNF/CNC film forming mechanism, properties and provide a technical basis for the other potential applications such as packaging, biomedical fields.

The aim of this study was to tailor the properties of thin nanocellulose films by controlling the weight ratios of CNFs and CNCs in the suspensions. The suspension rheology, and thermal, mechanical, optical properties and crystalline structure of the prepared films were investigated. A commercial porous PBS film (25 μm thick) was used for a comparative purpose. The CNFs and CNCs were prepared using the acid hydrolysis method, and the thin nanocellulose films were prepared using vacuum filtration method. Rheological and zeta potential properties of different CNF/CNC suspensions were tested to demonstrate the film forming mechanisms. The CNF/CNC films were characterized through morphology, thermal, X-ray diffraction, optical transmittance, and tensile strength analysis.

Materials and methods

Materials

Bleached KC Flock W-50 wood pulp fibers were purchased from Nippon Paper Chemicals (Tokyo, Japan). Concentrated sulfuric acid (99.9%) was from

EMD Millipore Corporation (Darmstadt, Germany), which was diluted to 64 and 48% for preparing CNCs and CNFs, respectively. Milli-Q deionized water was provided by Merck Company (Darmstadt, Germany). Dialysis Tubing with molecular weight cut-off 12,000–14,000 made from regenerated cellulose membrane was purchased from Fisher Scientific (Pittsburgh, USA). Microporous tri-layer PBS film was purchased from the MTI Corporation (Richmond, USA) and the ratio of polyethylene (PE) and polypropylene (PP) was estimated to be about 45:55%.

Preparation of CNCs and CNFs

A 1:10 weight ratio of pulp to acid was used to prepare cellulose nanomaterials. More specifically, target amount of bleached wood pulp was added to the 64 or 48% of sulfuric acid solution at 45 °C to prepare CNCs and CNFs, respectively, with rigorously stirring for 1 h. Then, ten folds of DI water were added to the reaction system to discontinue the hydrolysis process. The excessive sulfuric acid in the diluted suspension was removed using a high-speed centrifuge at 9000 r/min and the material was rinsed with deionized water 3 times. The hydrolyzed fibers were collected and re-dispersed in the deionized water. The nanocellulose suspension were placed in a dialysis tubing and dialyzed for 3–5 days until a PH value of 7.0 was obtained. To make the nanocellulose homogeneously distributed in the aqueous system, the hydrolyzed nanofiber suspension was homogenized by a Microfluidizer M-110EH-30 Processor for 3–5 times under an operation pressure of 202 MPa.

Preparation of ultrathin CNF/CNC film

The ratios of CNF/CNC in the formed films are shown in Table 1. The letters “C” and “F” denote CNCs and CNFs, respectively. The numbers represent the mixing ratio of CNFs and CNCs in the CNF/CNC film. For example, C1F1 denotes 50% CNCs and 50% CNFs, and C3F1 means 75% CNCs and 25% CNFs. Before the film preparation process, the aqueous CNF/CNC suspensions were sonicated by an ultrasonic homogenizer (MSK-USP-12 N, MTI Corporation, Richmond, USA) for about half an hour with 3 min intermissions between each 10 min. Thin CNF/CNC films were prepared using the vacuum filtration method with a DVPP membrane (pore size:

0.65 μm). The obtained wet sheets were dried at about 95 °C for about 30 min in a vacuum oven.

Suspension and film property characterization

The rheology properties of CNF/CNC suspensions (0.5 wt% in isopropyl alcohol) were characterized with an AR2000ex stress controlled rheometer at room temperature. The cone angle and diameter of the test geometry were 2° and 60 mm, respectively. A JEOL 100CX transmission electron microscope was used to conduct the morphology analysis of CNFs or CNCs. The zeta (ζ) potentials of CNF/CNC suspensions (0.5 wt%) were measured by a MicroTrac ZetaTrac analyzer equipped with a dynamic light scattering system at room temperature. A FEI field-emission SEM was used to analyze the morphology of the CNF/CNC and PBS films under 5 kv and 3.9 Pa. The thermal stability of the CNF/CNC film was studied using a Q50 TGA under N₂ atmosphere with a temperature range of 30–600 °C. The specific weight-loss rate of each sample was read from the derivative thermogravimetric (DTG) curve. A TA Q400 thermomechanical analyzer (TMA) equipped with a film/fiber probe was used to test the coefficients of thermal expansion (CTE) of the CNF/CNC film in tensile mode. The CTE was determined by the slope of the expansion percentage ($\Delta L/L_0$) versus temperature. The temperature used in CTE tests was increased from 20 to 120 °C at a rate of 3 °C/min. The XRD patterns of these films were recorded with a Bruker/Siemens D5000 X-ray diffractometer. The accelerating voltage and current were set at 45 kV, 40 mA. Both Segal's method (Segal et al. 1959) and the peak deconvolution method (Terinte et al. 2011) were utilized to calculate the crystallinity index (CrI, %) of the samples. The Segal's method has the following form:

$$\text{CrI}(\%) = 100 * (I_{200} - I_{am})/I_{200} \quad ([1])$$

where I_{am} is the diffraction intensity associated with amorphous regions of cellulose, I_{200} is the maximum intensity of the principal peak. The peak deconvolution method has the following form:

$$\text{CrI} = \frac{I_{cr \text{ peak } 1} + I_{cr \text{ peak } 3} + I_{cr \text{ peak } 4}}{I_{cr \text{ peak } 1} + I_{cr \text{ peak } 3} + I_{cr \text{ peak } 4} + I_{non-cr}} \times 100\% \quad ([2])$$

where $I_{cr \text{ peak}}$, and I_{non-cr} denotes the area under the

Table 1 Sample formulation, onset decomposition temperature (T_{onset}), maximum thermal decomposition temperature (T_{max}), maximum weight loss rate (WLR_{max}), coefficient ofthermal expansion (CTE), crystalline index (CrI), maximum tensile strength (σ_{max}) and zeta potential (ζ) of the CNF/CNC and PBS films

Sample type	Content (%)		T_{onset} (°C)	T_{max} (°C)	WLR_{max} (%) min	CY (%)	CTE (ppm/ K)	CrI ^a (%)	σ_{max} (MPa)	ζ (mV)
	CNC	CNF								
C1	100	0	300	321	1.87	24.12	11.86	62.17	150.4	− 43.5
C3F1	25	75	304	327	1.75	22.31	13.30	59.32	146.5	− 36.2
C1F1	50	50	311	333	1.65	20.82	14.74	57.09	142.4	− 23.1
C1F3	75	25	312	340	1.60	15.19	15.22	52.62	138.4	− 13.2
F1	0	100	319	358	1.35	10.60	17.65	50.23	133.9	− 7.6
PBS	–	–	340	455	2.19	0.003	178.90	–	15.2 (TD)	–

^aThe C_rI values shown are from the peak deconvolution method. The corresponding data from Segal's methods are 64.37, 63.02, 61.06, 60.47, and 60.19% for C1, C3F1, C1F1, C1F3, and F1, respectively

crystalline peak and non-crystalline peak, respectively. Tensile strength of CNF/CNC film was determined using an Instron 5582 testing machine according to the ASTM D638-03 standard. A one KN load cell was used with miniature tensile grips and the loading speed was 5 mm/min. The porosity of the nanocellulose and PBS films were measured by using the weight difference prior and after the absorption of electrolyte in a glove box, and calculated by the following equation (Zhang et al. 2015b):

$$\text{porosity}(\%) = (w_a - w_b) / (\rho_e \times v_s) \times 100\% \quad ([3])$$

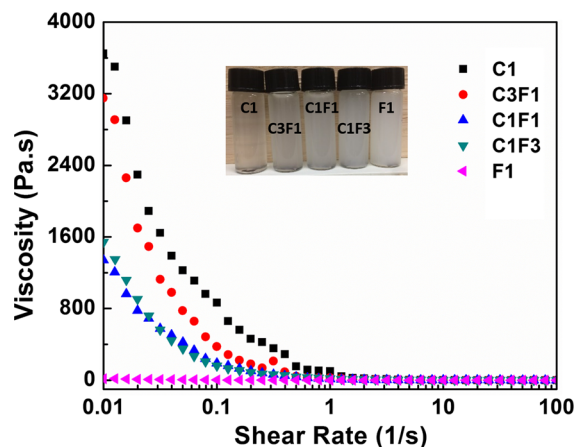
where W_a and W_b are the weights of the films before and after soaking in the electrolyte, ρ_e is the density of electrolyte and V_s is the volume of the film.

Results and discussion

Suspension rheology behavior

The viscosity of CNF/CNC suspension has a great influence on the quality of the formed film. High viscosity led to difficulty in eliminating bubbles in the suspension, resulting in inconsistent film quality and decreased mechanical and optical properties. The viscosity-shear rate curve of CNF/CNC suspension at low concentration is shown in Fig. 1.

The nanocellulose suspensions exhibited a typical shear-thinning behavior at low shear rate region ($< 10 \text{ s}^{-1}$). The phenomenon was due to the disruption of intra-nanocellulose (or cellulose fibril)

**Fig. 1** Typical viscosity-shear rate curves of the CNF/CNC suspensions

junctions with the increase of shear rate, which indicated that CNF/CNC suspensions showed entanglement network system behavior (El Miri et al. 2015). This behavior was further confirmed by the morphology analysis of freeze dried samples discussed in the next section. Even though the mean length of CNFs was larger than that of CNCs, CNCs showed a larger viscosity value compared with that of the CNFs at the lower shear rate region ($0.01\text{--}1 \text{ s}^{-1}$). For example, the viscosity of C1, C3F1, C1F1, C1F3, and F1 were approximately 101.6, 27.71, 20.85, 13.05, and 0.219 Pa s, respectively. With the increased ratio of CNCs in the suspension, the viscosity value also increased. This phenomenon was attributed to the CNC's self-assembly phase (i.e., chiral nematic liquid

crystalline phase) and the hydrogen bonding interactions among nanocellulose fibers (Salas et al. 2014). Many factors influence the nematic phase formation, including surface charge, chiral structure of cellulose chains, and twisting conditions of CNCs. During the hydrolysis process, higher sulfuric acid concentration was used to prepare CNCs than that used for CNFs (i.e., 64% for CNCs vs 48% for CNFs). Since the surface charge of nanocellulose was mainly due to the introduction of sulfate half-ester groups in the hydrolysis process, CNCs had a larger surface charge than CNFs as shown in Table 1. The ζ -potential of CNCs and CNFs were -43.5 mV and -7.6 mV, respectively. The larger surface charge provided the electrostatic repulsion force and helped suspend CNCs homogeneously in the aqueous system, while CNFs aggregated much easier. After CNF suspensions were stored for several days, the phase separation phenomenon occurred. The CNC suspensions remained stable for a much longer time period. This phenomenon can also explain why the viscosity of CNF suspensions was smaller than that of CNC suspensions at low shear rate region. At the higher shear rate region ($> 10 \text{ s}^{-1}$), the viscosity remained nearly stable ($< 1 \text{ Pa s}$) with the increase of shear rate, which indicated that CNF and CNC suspensions exhibited the Newtonian fluid behavior. Both CNFs and CNCs had similar viscosity values because the CNF/CNC entanglement network system was disrupted thoroughly in the rotational testing process under higher shear speeds, which helped CNCs and CNFs suspend homogeneously. Thus, CNC and CNF suspensions exhibited different viscosity behaviors at different shear-rate regions.

Morphology properties

The TEM images of CNCs/CNFs and SEM images of freeze-dried nanocellulose samples are shown in Fig. 2. CNCs had a rod-like shape (Fig. 2a), whereas CNFs had a fibril shape (Fig. 2b).

The average diameter of CNCs and CNFs were 9.1 ± 2.3 , $21.3 \pm 9.6 \text{ nm}$, respectively. The relevant mean aspect ratios were approximately 12.6 for CNCs and 106.7 for CNFs based on measurements from TEM images (Fig. S1). The aspect ratio values of CNFs exhibited a much larger variability (up to 210) than that of CNCs, which was mainly due to a larger variance of the CNF length. The diameter and length of CNFs were obviously larger than these of CNCs due

to different hydrolysis process. The disordered regions in the cellulose molecule chains were increasingly removed at the higher sulfuric acid concentration level (64 wt%), which led to reduced size of CNCs (Sofla et al. 2016). The samples exhibited in Fig. 2c–f were freeze-dried samples at 0.5 wt% concentration. Figures 2c–d show how CNCs were attached to CNFs in the mixture. Due to the different shape and length of CNCs and CNFs, they exhibited different behavior during film forming process. Because of the smaller length of CNCs, CNC films inclined to form ordered layer structure (Fig. 2e). The phenomenon was attributed to the self-assembly of CNCs during the drying process (Han et al. 2013). However, due to the entangled CNFs, it was much easier for CNFs to form amorphous network (Fig. 2f). These different film forming mechanisms influence their optical and mechanical properties.

The SEM images of CNF/CNC and PBS films are shown in Fig. 3. Due to the different size and shape of CNCs and CNFs, different film morphologies were observed. Different layers of CNCs were stacked together in pure CNC film. With the addition of CNFs, more and more pores were formed (Fig. 3a–f). Pure CNF films did not show a layer structure, but exhibited a porous network. This was attributed to the large length of CNFs, which entangled together during the homogenization process. The ordered slit pores in PBS film are clearly observed from the Fig. 3f. This can be explained by the uniaxial stretching during the film manufacturing process, which greatly influenced its mechanical performance (Lee et al. 2014).

Film thermal stability

The TGA curves of the thin CNF/CNC and PBS films are shown in Fig. 4. For CNF/CNC films, the weight loss at low temperature range (below 100°C) was due to the evaporation of the water (Nagalakshmaiah et al. 2016).

The thin nanocellulose films remained stable until about 300°C (Fig. 4a). The onset decomposition temperature (T_{onset}), maximum thermal decomposition temperature (T_{max}), weight loss (WL) of these samples are shown in Table 1. Both values of T_{onset} and T_{max} were shifted to high temperature region when the proportion of CNFs added in the CNF/CNC film was increased. For example, the corresponding value of T_{max} for C1, C3F1, C1F1, C1F3 and F1 were 321,

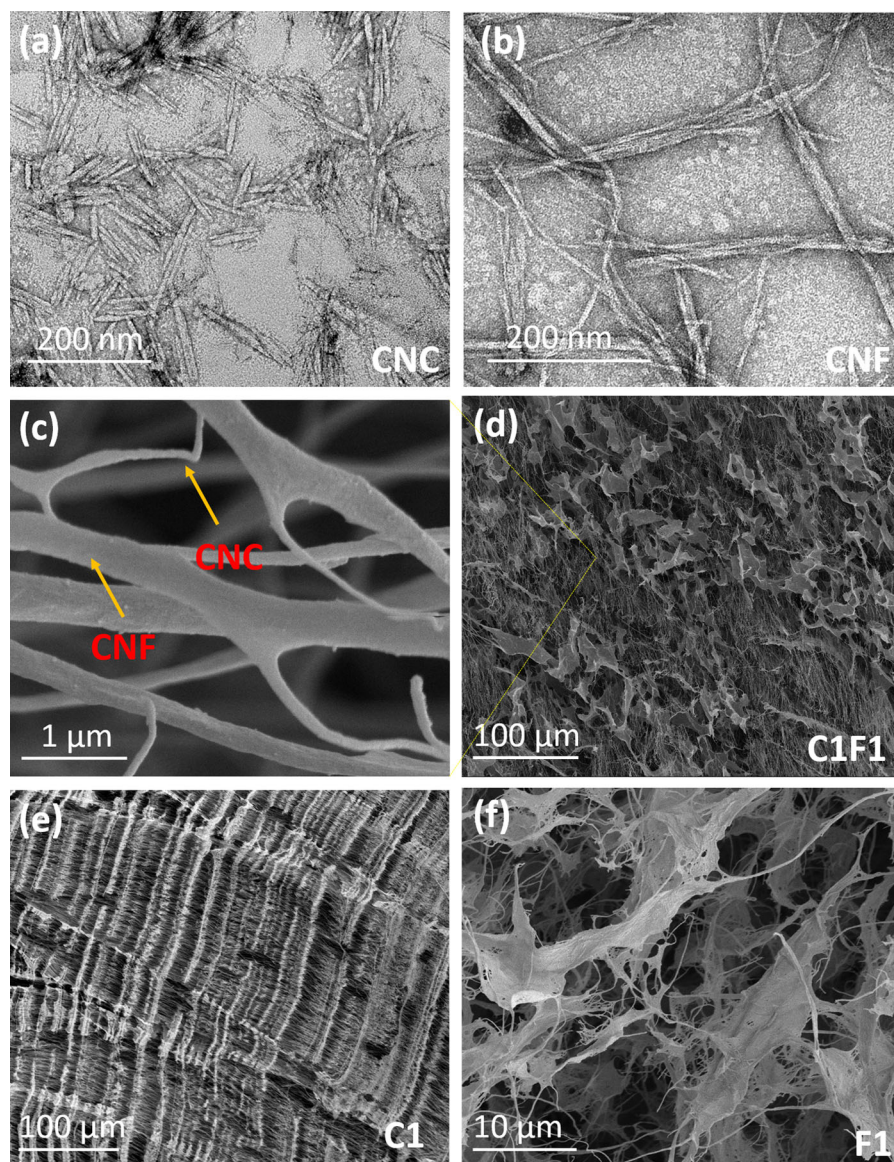


Fig. 2 Micrographs of nanocellulose and its films. **a** CNCs; **b** CNFs; **c** C1F1 (high magnification); **d** C1F1 (low magnification); **e** layer structure of C1; and **f** network structure of F1

327, 333, 340 and 358 °C, respectively (Fig. 4b). The values of T_{onset} and WLR_{max} exhibited the same trend. The reason of this shift was due to the different morphologies of CNFs and CNCs. The surface area of CNCs was larger than that of CNFs, because the particle size difference between CNFs (length: 0.5–2 μm) and CNCs (length: 0.05–0.5 μm). In addition, different concentrations of sulfuric acid were used to produce CNFs (48% H_2SO_4) and CNCs (64% H_2SO_4). The thermal stabilities of CNFs or CNCs

were reduced by the acid hydrolysis due to the introduction of sulfate groups (de Morais Teixeira et al. 2010). During the thermal decomposition process, these sulfate groups functioned like a catalyst, which facilitated the dehydration process. In addition, some hydroxyl groups at the surface of cellulose microfibrils were replaced by the sulfate groups and this replacement decreased the onset decomposition temperature. Thus CNCs showed an earlier pyrolysis phenomenon and larger maximum weight loss rate

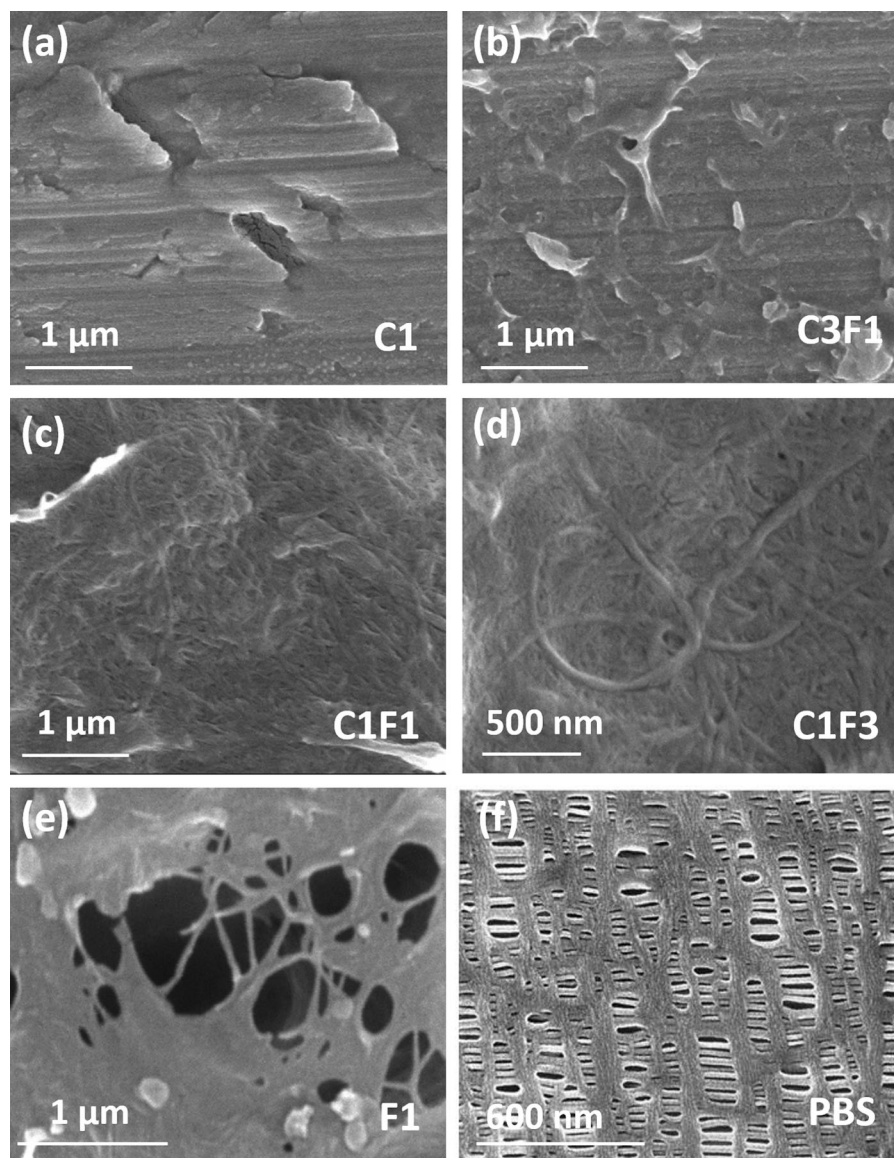


Fig. 3 SEM images of CNF/CNC and PBS films. **a** C1; **b** C3F1; **c** C1F1; **d** C1F3; **e** F1; and **f** PBS

compared with CNFs. Another interesting phenomenon was that the char yield showed an opposite trend, which decreased from 24.12% for pure CNC film to 10.60% for pure CNF film. This phenomenon was mainly due to smaller size of CNCs, which form early char layer to protect the rest of material (Kumar et al. 2014). PBS film began to decompose at about 340 °C, and the maximum weight loss rate (2.19%/min) peaked at 455 °C with nearly no residue left (CY = 0.003%). DSC analysis results of PBS film showed that two endothermic peaks were observed

(the small insert figure in Fig. 4a), which showed the melting temperatures of polyethylene (PE) and polypropylene (PP) at about 134.73 °C, and 164.28 °C, respectively. The ratio of (45:55%) PE and PP was estimated from the peak height ratio from FTIR spectra (Fig. S2). The CH₃ or CH₂ group of PP and PE appeared at 1372 and 1455 cm⁻¹, respectively. As shown in Fig. S3, both CNF film and PBS film remained stable at the low temperature. When the temperature was increased to about 170 °C, the PBS

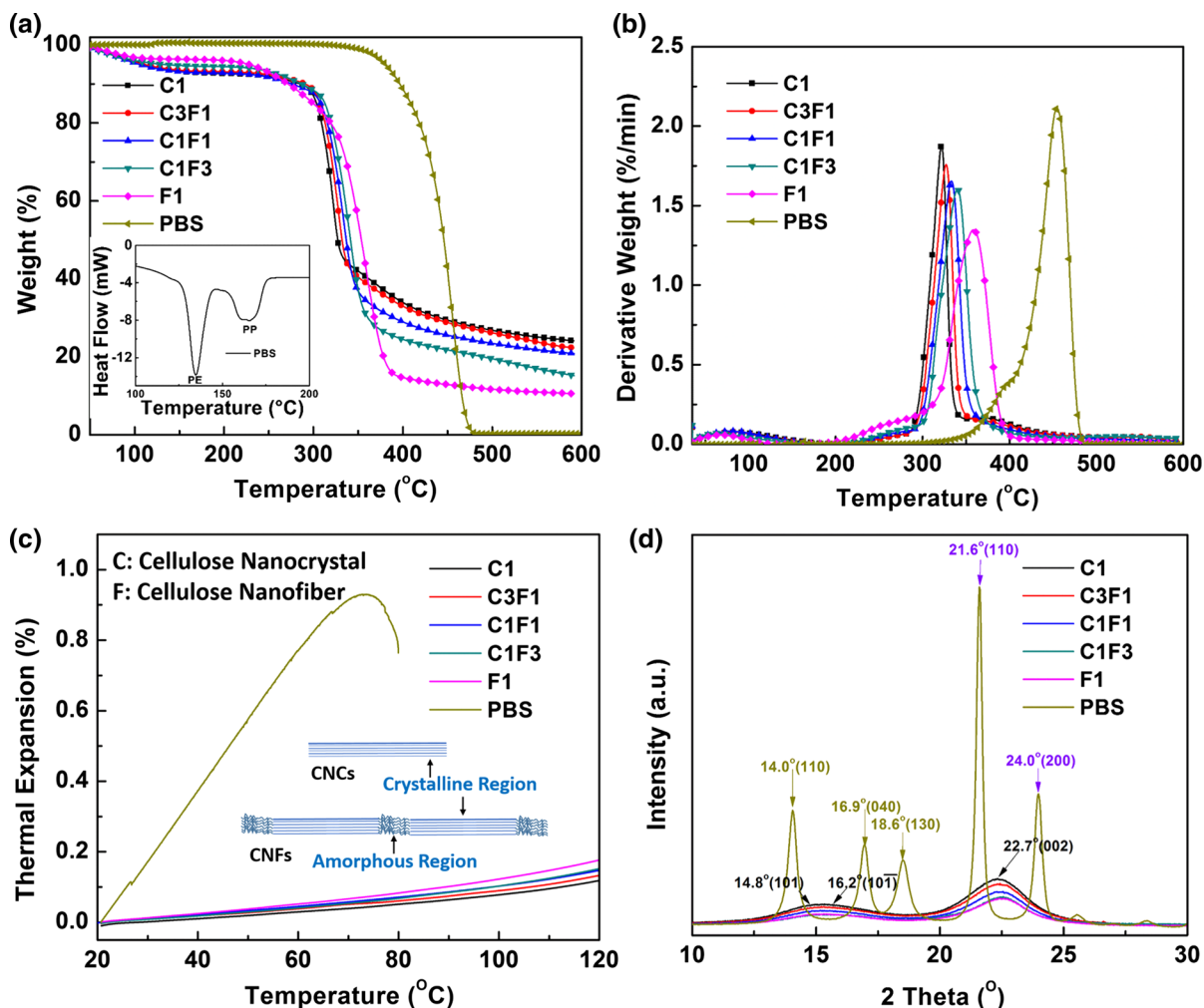


Fig. 4 Thermal stability property and X-ray diffraction spectra of the CNF/CNC film in comparison with PBS film. **a** TGA; **b** DTG; **c** thermal expansion; and **d** XRD spectra

film melted in 15 s while nothing unusual was observed in the CNF film.

Film thermal expansion behavior

The coefficient of thermal expansion (CTE) plays an important role when thin films are used in green electronic or composites fields. The large CTE values and CTE mismatches among various components can result in the malfunction of electronic devices and the deterioration of the mechanical performance of composites (Diaz et al. 2013). CNF/CNC films exhibited a much smaller thermal expansion (< 0.17%) between 20 and 120 °C (Fig. 4c and Table 1). The value of CTE also became larger when the ratio of CNFs was

increased in the nanocellulose film. For example, the CTE values for C1, C1F1, and F1 were 11.86, 14.74, and 17.65 ppm/k, respectively. This phenomenon was attributed to the different structure of CNFs and CNCs (schematic picture shown in Fig. 4c). Another reason for this difference was due to the different arrangements of the CNCs/CNFs in the nanocellulose film. As mentioned before, CNCs exhibited nematic behavior or more specifically, liquid crystalline behavior due to the aspect ratio and rigid of CNCs (Moon et al. 2011). CNFs did not show this property due to their smaller stiffness and larger length. CNCs behaved similarly to rods whereas CNFs showed worm-like behavior, which resulted in different packing arrangements in the dried film. PBS film exhibited a much larger CTE

value (178.90 ppm/k) when compared with that of the ultrathin nanocellulose film (11.86–17.65 ppm/k). Due to the low melting temperature of PP (130–171 °C) and PE (about 80–135 °C), PBS film firstly expanded 0.926% between 20 and 74 °C, and then it began to shrink. Both PP and PE are thermoplastic polymers, and they are linked together through van der Waals forces or intermolecular bonding. The large CTE of PBS film was mainly caused by the decrease of modulus when the testing temperature increased from room temperature to 80 °C (Orchard et al. 1984). The value of CTE became negative above 70 °C, ascribed by the formation of shrinkage force during the melting process of PBS film.

Film crystalline structure

All the five thin nanocellulose films showed the cellulose I β crystalline structure with different intensities (Fig. 4d). The three main characterization peaks were observed at 14.8° (110), 16.2° (1 1 $\bar{1}$ 0) and 21.6° (200), respectively (Sun et al. 2015). More specifically, the lattice vectors of the monoclinic unit cells were 7.78, 8.20, 10.38 Å and the inter-axial angle (γ) was about 96.55° (French 2014). The crystalline structure of cellulose was formed by the inter/intra molecular H-bonding and van der Waals interactions among different microfibrils (Johar et al. 2012). Another phenomenon observed from Fig. 4d was that these peaks corresponded to the crystalline structure were increased with the addition of the CNCs into CNFs. The CrI values of these samples were increased from 50.23% (pure CNFs), 57.09% (CNFs:CNCs = 1:1) to 62.17% (pure CNCs). The CrI data from the Segal's method showed a similar trend, but had smaller values as previously discussed (Park et al. 2010). The data trend was understandable because the amorphous region of the nanocellulose fibrils was removed when 64% sulfuric acid was used to prepare CNCs. Despite that, the acid hydrolysis process with a larger acid concentration may also help realign the crystalline regions in parallel and finally increased the CrI value of CNCs (de Moraes Teixeira et al. 2010). The corresponding CrI value increased with the increase of CNC ratio in the CNF/CNC film. The increase of CrI value also influenced the mechanical properties of CNF/CNC films as discussed in the film mechanical performance section. Both the characteristic peaks of PP and PE

were observed from the spectra of the commercial PBS film. The commercial PBS film exhibited a higher crystallinity due to their intense characterization peaks (Furukawa et al. 2006). Two intensive peaks of PE were found at 21.6° (110), and 24.0° (002) (Zhang et al. 2015c). The crystal planes for PP were found at 14.0° (110), 16.9° (040) and 18.6° (130), respectively, which showed that PP exhibited a typical α -form (Lin et al. 2015). Compared to the crystallinity peak of PBS, the peak intensity of CNF/CNC was much smaller. This was due to the different source materials. PBS was composed of PP and PE which were artificially synthesized polymers and had a great degree of polymerization (DOP) whereas CNFs/CNCs were biosynthesized natural materials and the DOP were ranged from 10,000 to 15,000.

Film optical transmittance

Optical property of nanocellulose films helps determine whether these films are suitable for use in the “green electronics” or food packaging fields. The CNC films exhibited the best optical transmittance compared with the other film. With the addition of CNFs in the film, the transmittance declined gradually. For instance, the transmittance of C3F1 film was about 41.8% at 600 nm, whereas the value decreased to 36.5, 14.667 and 8.2% for C1F1, C1F3, and F1, respectively (Fig. 5a). This phenomenon was mainly attributed to the different size and shape of CNCs and CNFs. According to the Rayleigh's Scattering theory, the scattering cross section is directly proportional to the fiber diameter ($\sigma_{sca} \propto D$) (Zhu et al. 2014). With the increase of nanocellulose diameter or width, the amount of light scattered also increased significantly, which resulted in the decrease of optical transmittance (Lizundia et al. 2016). As shown in Fig. 2, CNCs showed a rod-like shape, and the average diameter and length of CNCs were about 20 nm, and 160 nm, respectively. For CNFs, their diameter differed greatly in a range from 10 to 100 nm and the length was up to several micro meters. In addition, the distribution of CNFs/CNCs in the nanocellulose film matrix also had a significant impact on the transparency. Due to larger length of CNFs, there fibers easily entangled together and formed a complex network structure. The CNCs in CNC-based films exhibited a better alignment, leading to a good degree of homogeneity of nanocellulose film (Cheng et al. 2016). These different types of internal

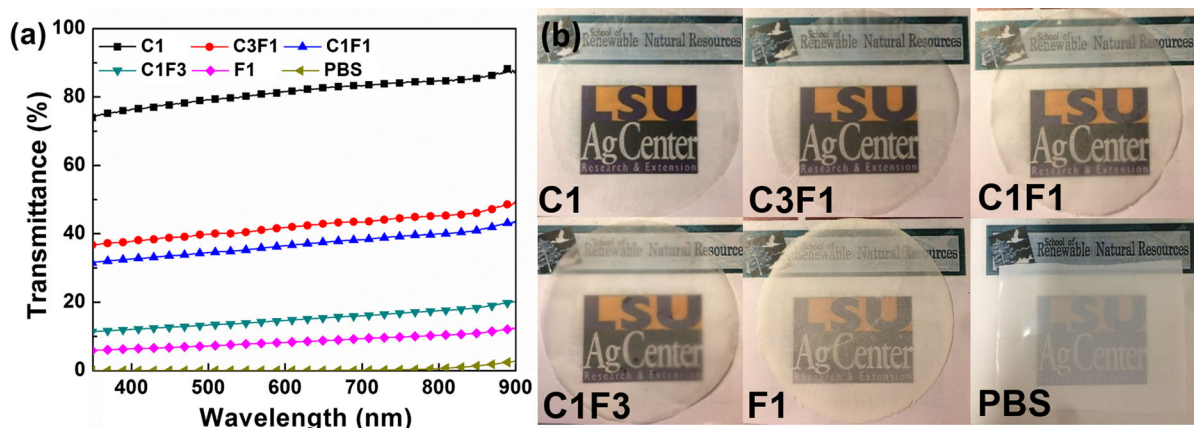


Fig. 5 Optical properties of CNF/CNC and PBS films. **a** UV-Vis transmittance spectra; and **b** optical transparency

microstructures tailored the light scattering and optical transmittance. Thus, it is hard for light to transmit through CNF films.

The optical transmittance of PBS film was very low, which was less than 2.7%. This phenomenon was due to the structure, polymer source and manufacture method used. The UV-Vis transmittance measurements of these films were consistent with the corresponding visual observations as shown in Fig. 5b. With the increased ratio of CNFs in the nanocellulose films, the amount of light scattering increased and the patterns behind the films became blur. The optical transmittance of PBS film was very low (less than 2.7%), due to the sandwiched structure, polymer source, and manufacture methods used.

Film mechanical performance

Typical tensile strain–stress curves of CNF/CNC and PBS films are shown in Fig. 6. CNF/CNC and PBS films exhibited similar maximum tensile stress (about 150 MPa) at the break. PBS membrane had a much larger elongation at break than these of nanocellulose films. The maximum tensile strength increased with the ratio of CNCs/CNFs. For example, the corresponding value of tensile stress for C1, C1F1, F1 were 150.4, 142.4, and 133.9 MPa, respectively (Fig. 6a and Table 1). This phenomenon was attributed to the different components of CNFs and CNCs. CNFs contained both amorphous and crystalline regions, whereas most amorphous regions of cellulose were removed for CNCs. The crystalline region had a better alignment and larger modulus than these of the

amorphous region. Another reason was due to the different surface area of CNCs and CNFs. As described in the morphology analysis section, the size of CNCs was smaller than that of CNFs. The main mechanical strength of nanocellulose films were formed by the hydrogen bonds between different cellulose fibrils during the water removal process and the friction forces of the entangled network (Mao et al. 2017), which were created in the film-forming procedure. As shown in Fig. S2, the broad band between 3600 and 3200 cm^{-1} was assigned to hydrogen bond OH stretching. The small band at 3336 cm^{-1} corresponded to the intramolecular hydroxyl groups (3 – OH...O – 5). The intermolecular hydrogen bonds (6 – OH...O – 3') appeared at 3302 cm^{-1} (Yue et al. 2015). Large surface area led to more hydrogen bonds and larger friction forces. Another reason, which can help explain the decrease of the maximum tensile stress for C1, C1F1, and F1, was the increase of porosity. The porosity of C1, C3F1, C1F1, C1F3, and F1 were 10, 16, 27, 31, and 49%, respectively. The commercial separator film had a porosity of about 39%.

The value of the tensile strain exhibited an opposite trend. With the increased ratios of CNCs in nanocellulose film, the smaller tensile strain values were obtained. The tensile strain to failure for pure CNC and CNF films were about 7.8 and 8.9%. This was due to the amorphous region in the CNFs, which could sustain more tensile force during the tensile testing. During the elongation process, these fibrils in the amorphous regions were extended and rearranged, which led to the regeneration of intramolecular

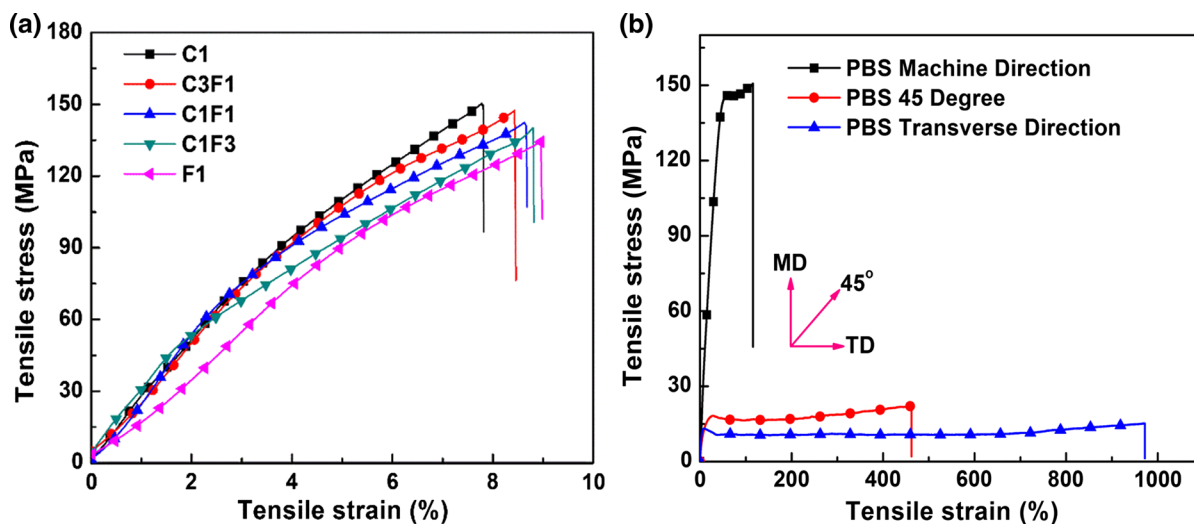


Fig. 6 Typical tensile strain–stress curves of the test films. **a** CNF/CNC, and **b** PBS

H-bonds and improvement of the elongation at break at break (Zhang et al. 2015a).

Another mechanical difference between nanocellulose film and PBS membrane is that PBS showed different tensile strength at different directions (Fig. 6b), whereas nanocellulose film had more uniform properties. Along the machine direction (MD), the tensile stress and strain at break for PBS membrane were about 150.6 MPa and 115.7%. At the transverse direction (TD), the corresponding values were 15.2 MPa and 972.2%. At the direction between MD and TD (45°), the corresponding values were about 22.1 MPa and 462.2%. This phenomenon was ascribed by the specific manufacturing method. These sources materials such as PP or PE were melted, extruded to form sheet and then thermally annealed to increase the amount and size of lamella crystallites. In order to induce ordered slit-like microporous structure, the obtained PBS sheet with stacked lamellae crystallites was uniaxially stretched. Due to the uniaxial stretching process, the PBS film exhibited anisotropy. However, nanocellulose film did not have this detrimental effect, because nanocellulose formed network during the drying process as shown in Fig. 2.

Conclusions

Thin CNF/CNC films were successfully made and their fundamental properties were characterized and

analyzed. Different rheological properties were observed for different ratios of CNF/CNC suspensions. CNFs and CNCs exhibited different film forming mechanism due to the differences in morphology, aspect ratio, and zeta potential. Compared with the reference-PBS film, CNF/CNC films exhibited better performance in thermal stability and thermal expansion behavior. With the increased addition of CNCs, the viscosity of nanocellulose suspension, and the crystalline index, zeta potential, tensile strength, and optical transparency of the film were increased. The porosity, thermal stability, and thermal expansion were increased with the increasing ratio of CNFs. The CNF/CNC film remained thermally stable up to 340 °C and expanded less than 0.17% (11.86–17.65 ppm/k) between 20 and 120 °C. The PBS film was melt at 135 °C and expanded about 0.926% (178.90 ppm/k) between 20 and 74 °C. The best optical transmittance performance was obtained from C1 film (75–88% transmittance at 300–900 nm region). In addition, PBS film demonstrated much different maximum tensile strength at break at different directions (MD: 150.6 MPa, TD: 15.2 MPa). The CNF/CNC films had more uniform strength along both directions. This study provides a new method to control the specific properties of nanocellulose film using combined CNF and CNC suspension. Our future work will demonstrate the use of such films in energy storage devices.

Acknowledgments This study was carried out with support from Louisiana Board of Regents [LEQSF(2017-18)-RD-A-01], LEQSF(2015-17)-RD-B-01], LSU Economic Development Assistantship Program, Henan Agricultural University (Zhengzhou, China), and Henan Academy of Science (Zhengzhou, China).

References

- Abdalkarim SYH, Yu H-Y, Wang D, Yao J (2017) Electrospun poly(3-hydroxybutyrate-co-3-hydroxy-valerate)/cellulose reinforced nanofibrous membranes with ZnO nanocrystals for antibacterial wound dressings. *Cellulose* 24:2925–2938. <https://doi.org/10.1007/s10570-017-1303-0>
- Alam MM, Mandal D (2016) Native cellulose microfiber-based hybrid piezoelectric generator for mechanical energy harvesting utility. *ACS Appl Mater Interfaces* 8:1555–1558. <https://doi.org/10.1021/acsami.5b08168>
- Cheng S, Zhang Y, Cha R, Yang J, Jiang X (2016) Water-soluble nanocrystalline cellulose films with highly transparent and oxygen barrier properties. *Nanoscale* 8:973–978. <https://doi.org/10.1039/C5NR07647A>
- Chun S-J, Choi E-S, Lee E-H, Kim JH, Lee S-Y, Lee S-Y (2012) Eco-friendly cellulose nanofiber paper-derived separator membranes featuring tunable nanoporous network channels for lithium-ion batteries. *J Mater Chem* 22:16618–16626. <https://doi.org/10.1039/C2JM32415F>
- Costa SV, Pingel P, Janietz S, Nogueira AF (2016) Inverted organic solar cells using nanocellulose as substrate. *J Appl Polym Sci* 133:43679–43685. <https://doi.org/10.1002/app.43679>
- de Moraes Teixeira E, Corrêa AC, Manzoli A, de Lima Leite F, de Oliveira CR, Mattoso LHC (2010) Cellulose nanofibers from white and naturally colored cotton fibers. *Cellulose* 17:595–606. <https://doi.org/10.1007/s10570-010-9403-0>
- Diaz JA, Wu X, Martini A, Youngblood JP, Moon RJ (2013) Thermal expansion of self-organized and shear-oriented cellulose nanocrystal films. *Biomacromol* 14:2900–2908. <https://doi.org/10.1021/bm400794e>
- El Miri N, Abdelouahdi K, Barakat A, Zahouily M, Fihri A, Solhy A, El Achaby M (2015) Bio-nanocomposite films reinforced with cellulose nanocrystals: rheology of film-forming solutions, transparency, water vapor barrier and tensile properties of films. *Carbohydr Polym* 129:156–167. <https://doi.org/10.1016/j.carbpol.2015.04.051>
- Fang Z et al (2014) Novel nanostructured paper with ultrahigh transparency and ultrahigh haze for solar cells. *Nano Lett* 14:765–773. <https://doi.org/10.1021/nl404101p>
- French AD (2014) Idealized powder diffraction patterns for cellulose polymorphs. *Cellulose* 21:885–896. <https://doi.org/10.1007/s10570-013-0030-4>
- Furukawa T et al (2006) Molecular structure, crystallinity and morphology of polyethylene/polypropylene blends studied by raman mapping, scanning electron microscopy, wide angle X-ray diffraction, and differential scanning calorimetry. *Polym J* 38:1127–1136
- Garusinghe UM, Varanasi S, Garnier G, Batchelor W (2017) Strong cellulose nanofibre–nanosilica composites with controllable pore structure. *Cellulose* 24:2511–2521. <https://doi.org/10.1007/s10570-017-1265-2>
- Habibi Y, Lucia LA, Rojas OJ (2010) Cellulose nanocrystals: chemistry, self-assembly, and applications. *Chem Rev* 110:3479–3500. <https://doi.org/10.1021/cr900339w>
- Han J, Zhou C, Wu Y, Liu F, Wu Q (2013) Self-assembling behavior of cellulose nanoparticles during freeze-drying: effect of suspension concentration, particle size, crystal structure, and surface charge. *Biomacromolecules* 14:1529–1540. <https://doi.org/10.1021/bm4001734>
- Herrera MA, Sirviö JA, Mathew AP, Oksman K (2016) Environmental friendly and sustainable gas barrier on porous materials: nanocellulose coatings prepared using spin- and dip-coating. *Mater Des* 93:19–25. <https://doi.org/10.1016/j.matdes.2015.12.127>
- Herrera MA, Mathew AP, Oksman K (2017) Barrier and mechanical properties of plasticized and cross-linked nanocellulose coatings for paper packaging applications. *Cellulose* 24:3969–3980. <https://doi.org/10.1007/s10570-017-1405-8>
- Hollertz R, Durán VL, Larsson PA, Wågberg L (2017) Chemically modified cellulose micro- and nanofibrils as paper-strength additives. *Cellulose* 24:3883–3899. <https://doi.org/10.1007/s10570-017-1387-6>
- Hua K, Carlsson DO, Alander E, Lindstrom T, Stromme M, Mitranyan A, Ferraz N (2014) Translational study between structure and biological response of nanocellulose from wood and green algae. *RSC Adv* 4:2892–2903. <https://doi.org/10.1039/C3RA45553J>
- Johar N, Ahmad I, Dufresne A (2012) Extraction, preparation and characterization of cellulose fibres and nanocrystals from rice husk. *Ind Crops Prod* 37:93–99. <https://doi.org/10.1016/j.indcrop.2011.12.016>
- Kumar H, Christopher LP (2017) Recent trends and developments in dissolving pulp production and application. *Cellulose* 24:2347–2365. <https://doi.org/10.1007/s10570-017-1285-y>
- Kumar A, Negi YS, Choudhary V, Bhardwaj NK (2014) Characterization of cellulose nanocrystals produced by acid-hydrolysis from sugarcane bagasse as agro-waste. *J Mater Phys Chem* 2:1–8
- Lee H, Yanilmaz M, Toprakci O, Fu K, Zhang X (2014) A review of recent developments in membrane separators for rechargeable lithium-ion batteries. *Energy Environ Sci* 7:3857–3886. <https://doi.org/10.1039/C4EE01432D>
- Lin W-C, Lien C-C, Yeh H-J, Yu C-M, S-h Hsu (2013) Bacterial cellulose and bacterial cellulose–chitosan membranes for wound dressing applications. *Carbohydr Polym* 94:603–611. <https://doi.org/10.1016/j.carbpol.2013.01.076>
- Lin J-H et al (2015) Preparation and compatibility evaluation of polypropylene/high density polyethylene. *Polyblends Mater* 8:5496
- Linville E, Larsson PA, Östlund S (2017) Advanced three-dimensional paper structures: mechanical characterization and forming of sheets made from modified cellulose fibers. *Mater Des* 128:231–240. <https://doi.org/10.1016/j.matdes.2017.05.002>
- Lizundia E, Urruchi A, Vilas JL, León LM (2016) Increased functional properties and thermal stability of flexible cellulose nanocrystal/ZnO films. *Carbohydr Polym*

- 136:250–258. <https://doi.org/10.1016/j.carbpol.2015.09.041>
- Mao R, Goutianos S, Tu W, Meng N, Chen S, Peijs T (2017) Modelling the elastic properties of cellulose nanopaper. *Mater Des* 126:183–189. <https://doi.org/10.1016/j.matdes.2017.04.050>
- Moon RJ, Martini A, Nairn J, Simonsen J, Youngblood J (2011) Cellulose nanomaterials review: structure, properties and nanocomposites. *Chem Soc Rev* 40:3941–3994. <https://doi.org/10.1039/C0CS00108B>
- Nagalakshmaiah M, Kissi NE, Mortha G, Dufresne A (2016) Structural investigation of cellulose nanocrystals extracted from chili leftover and their reinforcement in cariflex-IR rubber latex. *Carbohydr Polym* 136:945–954. <https://doi.org/10.1016/j.carbpol.2015.09.096>
- Orchard GAJ, Davies GR, Ward IM (1984) The thermal expansion behaviour of highly oriented polyethylene. *Polymer* 25:1203–1210. [https://doi.org/10.1016/0032-3861\(84\)90364-1](https://doi.org/10.1016/0032-3861(84)90364-1)
- Park S, Baker JO, Himmel ME, Parilla PA, Johnson DK (2010) Cellulose crystallinity index: measurement techniques and their impact on interpreting cellulase performance. *Biotechnol Biofuels* 3(1):10
- Salas C, Nypelö T, Rodriguez-Abreu C, Carrillo C, Rojas OJ (2014) Nanocellulose properties and applications in colloids and interfaces. *Curr Opin Colloid Interface Sci* 19:383–396. <https://doi.org/10.1016/j.cocis.2014.10.003>
- Segal L, Creely JJ, Martin AE, Conrad CM (1959) An empirical method for estimating the degree of crystallinity of native cellulose using the X-ray diffractometer text. *Res J* 29:786–794. <https://doi.org/10.1177/004051755902901003>
- Shi X, Li C, Huang J, Wang W, Liu H, Xu Q (2016) Preparation and characterization of natural cellulose packaging film. In: Ouyang Y, Xu M, Yang L, Ouyang Y (eds) *Advanced graphic communications, packaging technology and materials*. Springer, Singapore, pp 827–835. https://doi.org/10.1007/978-981-10-0072-0_102
- Sofla MRK, Brown RJ, Tsuzuki T, Rainey TJ (2016) A comparison of cellulose nanocrystals and cellulose nanofibres extracted from bagasse using acid and ball milling methods. *Adv Nat Sci Nanosci Nanotechnol* 7:035004
- Sun X, Wu Q, Ren S, Lei T (2015) Comparison of highly transparent all-cellulose nanopaper prepared using sulfuric acid and TEMPO-mediated oxidation methods. *Cellulose* 22:1123–1133. <https://doi.org/10.1007/s10570-015-0574-6>
- Sun X, Wu Q, Lee S, Qing Y, Wu Y (2016) Cellulose nanofibers as a modifier for rheology, curing and mechanical performance of oil well cement. *Sci Rep* 6:31654. <https://doi.org/10.1038/srep31654>
- Terinte N, Ibbett R, Schuster KC (2011) Overview on native cellulose and microcrystalline cellulose I structure studied by X-ray diffraction (WAXD): comparison between measurement techniques. *Lenzinger Berichte* 89:118–131
- Xu X et al (2016) Highly transparent, low-haze, hybrid cellulose nanopaper as electrodes for flexible electronics. *Nanoscale* 8:12294–12306. <https://doi.org/10.1039/c6nr02245f>
- Xu Q, Wei C, Fan L, Peng S, Xu W, Xu J (2017) A bacterial cellulose/Al₂O₃ nanofibrous composite membrane for a lithium-ion battery separator. *Cellulose* 24:1889–1899. <https://doi.org/10.1007/s10570-017-1225-x>
- Yue Y, Han J, Han G, Zhang Q, French AD, Wu Q (2015) Characterization of cellulose I/II hybrid fibers isolated from energycane bagasse during the delignification process: morphology, crystallinity and percentage estimation. *Carbohydr Polym* 133:438–447. <https://doi.org/10.1016/j.carbpol.2015.07.058>
- Zhang B, Azuma J, Uyama H (2015a) Preparation and characterization of a transparent amorphous cellulose film. *RSC Adv* 5:2900–2907. <https://doi.org/10.1039/C4RA14090G>
- Zhang H, Wang X, Liang Y (2015b) Preparation and characterization of a lithium-ion battery separator from cellulose nanofibers. *Heliyon* 1:e00032. <https://doi.org/10.1016/j.heliyon.2015.e00032>
- Zhang X, Wu H, Guo S, Wang Y (2015c) Understanding in crystallization of polyethylene: the role of boron nitride (BN) particles. *RSC Adv* 5:99812–99819. <https://doi.org/10.1039/c5ra19982d>
- Zhang H, Yu H-Y, Wang C, Yao J (2017) Effect of silver contents in cellulose nanocrystal/silver nanohybrids on PHBV crystallization and property improvements. *Carbohydr Polym* 173:7–16. <https://doi.org/10.1016/j.carbpol.2017.05.064>
- Zhu H et al (2013) Biodegradable transparent substrates for flexible organic-light-emitting diodes. *Energy Environ Sci* 6:2105–2111. <https://doi.org/10.1039/C3EE40492G>
- Zhu H, Fang Z, Preston C, Li Y, Hu L (2014) Transparent paper: fabrications, properties, and device applications. *Energy Environ Sci* 7:269–287. <https://doi.org/10.1039/C3EE43024C>